

Brillouin Light Scattering of Halide Double Perovskite

Simin Pang, Xinbao Liu, Jiajun Luo, Yaru Xie, Jiang Tang, Sheng Meng,*
Ping-Heng Tan, and Jun Zhang*

$\text{Cs}_2\text{Ag}_{1-x}\text{Na}_x\text{In}_{1-y}\text{Bi}_y\text{Cl}_6$ with high photoluminescence quantum yield (PLQY) and broadband emission due to self-trapped excitons (STEs) is one of the promising candidates for single-emitter-based white light-emitting materials and devices. Considering fundamental physical mechanisms, structure design and performance optimization of devices, comprehensive knowledge of the elasticity, and thermal properties are imperative to understand the formation of STEs in $\text{Cs}_2\text{Ag}_{1-x}\text{Na}_x\text{In}_{1-y}\text{Bi}_y\text{Cl}_6$ and minimize thermomechanical stresses induced device failure, respectively. However, its elastic and thermal properties are still poorly understood. Herein, the first angle-resolved Brillouin light scattering (BLS) measurements study for a bulk $\text{Cs}_2\text{Ag}_{0.4}\text{Na}_{0.6}\text{InCl}_6:0.04\%\text{Bi}^{3+}$ crystal is reported, and the first-principles calculations of phonon dispersions are used to further validate our experimental results. Using the measured Brillouin frequency shifts, we evaluate the low elasticity of $\text{Cs}_2\text{Ag}_{0.4}\text{Na}_{0.6}\text{InCl}_6:0.04\%\text{Bi}^{3+}$: $C_{11} = 38.63$, $C_{12} = 16.11$, and $C_{44} = 10.20$ GPa, which supports the thesis that STEs exist in semiconductors with excitons and a soft lattice. Additionally, an ultralow-acoustic Debye temperature (87 K) and lattice thermal conductivity ($1.03 \text{ W m}^{-1} \text{ K}^{-1}$) along the [111] direction of $\text{Cs}_2\text{Ag}_{0.4}\text{Na}_{0.6}\text{InCl}_6:0.04\%\text{Bi}^{3+}$, which indicates the weak interatomic interactions and elasticity are estimated. Furthermore, a general approach is also provided to investigate the elastic and thermal properties of materials with different crystal structures utilizing angle-resolved BLS spectroscopy.

instability and the high toxicity of lead.^[3] Among all the lead-free halide perovskites, the halide double perovskites $\text{A}_2\text{M}^+\text{M}^{3+}\text{X}_6$ ($\text{A} = \text{Cs}^+$, MA^+ ; $\text{M}^+ = \text{Ag}^+$, Na^+ , In^+ ; $\text{M}^{3+} = \text{In}^{3+}$, Bi^{3+} , Sb^{3+} ; $\text{X} = \text{Cl}^-$, Br^- , I^-) have gained widespread attention for their characteristics of environmental friendliness, high photoluminescence quantum yield (PLQY), tunable emission across the visible spectrum, and low synthesis cost,^[4,5] which enable their potential applications in solar cells,^[6] light-emitting diodes (LEDs),^[7] photodetectors,^[8] and X-Ray detectors.^[9] Remarkably, a novel halide double perovskite $\text{Cs}_2\text{AgInCl}_6$ with direct bandgap^[10] has attracted great interest for its essential role in white light emission. With the strategies of doping and alloying, Tang's group found that $\text{Cs}_2\text{Ag}_{0.6}\text{Na}_{0.4}\text{InCl}_6$ bulk material with 0.04% bismuth doping ($\text{Cs}_2\text{Ag}_{0.6}\text{Na}_{0.4}\text{InCl}_6:0.04\%\text{Bi}^{3+}$) emits warm-white light (460–700 nm) with a prominently high PLQY of $(86 \pm 5)\%$.^[11] The Bi^{3+} incorporation improves the crystal perfection and exciton localization, further boosting the PLQY, while the introduction of Na^+ breaks the inversion-symmetry-induced parity-forbidden dipole transition and reduces the electronic dimensionality, leading to efficient broadband emission via radiative recombination of self-trapped excitons (STEs).^[11] Locardi et al. reported that Bi^{3+} -doped

1. Introduction

Recently, lead-free halide perovskites emerge to gradually replace the lead halide perovskites,^[1,2] which suffer from intrinsic

symmetry-induced parity-forbidden dipole transition and reduces the electronic dimensionality, leading to efficient broadband emission via radiative recombination of self-trapped excitons (STEs).^[11] Locardi et al. reported that Bi^{3+} -doped

S. Pang, Y. Xie, P.-H. Tan, J. Zhang
State Key Laboratory of Superlattices and Microstructures
Institute of Semiconductors
Chinese Academy of Sciences
Beijing 100083, China
E-mail: zhangjwill@semi.ac.cn

S. Pang, Y. Xie, P.-H. Tan, J. Zhang
Center of Materials Science and Optoelectronics Engineering
University of Chinese Academy of Sciences
Beijing 100049, China

 The ORCID identification number(s) for the author(s) of this article can be found under <https://doi.org/10.1002/adpr.202100222>.

© 2022 The Authors. Advanced Photonics Research published by Wiley-VCH GmbH. This is an open access article under the terms of the Creative Commons Attribution License, which permits use, distribution and reproduction in any medium, provided the original work is properly cited.

DOI: 10.1002/adpr.202100222

X. Liu, S. Meng
Beijing National Laboratory for Condensed Matter Physics
Institute of Physics
Chinese Academy of Sciences
Beijing 100190, China
E-mail: smeng@iphy.ac.cn

X. Liu, S. Meng
School of Physical Sciences
University of Chinese Academy of Sciences
Beijing 100049, China

S. Meng
Songshan Lake Materials Laboratory
Dongguan 523808, China

J. Luo, J. Tang
Wuhan National Laboratory for Optoelectronics (WNLO)
School of Optical and Electronic Information
Huazhong University of Science and Technology (HUST)
Wuhan 430074, China

$\text{Cs}_2\text{Ag}_{0.4}\text{Na}_{0.6}\text{InCl}_6$ nanocrystal shows PLQY of 22%.^[12] Subsequently, the PLQY of the $\text{Cs}_2\text{Ag}_{0.17}\text{Na}_{0.83}\text{In}_{0.88}\text{Bi}_{0.12}\text{Cl}_6$ nanocrystal was further promoted to 64% by Hu et al.^[13] Benefiting from the negligible self-absorption of STEs, Zhu et al. demonstrated high scintillator performance and X-Ray imaging based on $\text{Cs}_2\text{Ag}_{0.6}\text{Na}_{0.4}\text{In}_{1-y}\text{Bi}_y\text{Cl}_6$.^[14] Therefore, $\text{Cs}_2\text{Ag}_{1-x}\text{Na}_x\text{In}_{1-y}\text{Bi}_y\text{Cl}_6$ holds promise for single-emitter-based white light-emitting material and high-performance scintillator, and the related physical problems about the STEs would also be attractive. The STE is generally described as a bound electron-hole pair that couples to a soft lattice and then induces the large lattice deformations.^[15,16] Since the soft lattice that the crystal structure can be easily deformed under mechanical stress, that is, the weak elastic property is closely related to the STEs, investigating the elasticity of $\text{Cs}_2\text{Ag}_{1-x}\text{Na}_x\text{In}_{1-y}\text{Bi}_y\text{Cl}_6$ is significant to understand the mechanism of STEs formation and would suggest ways to control the STEs. In addition, Zhu et al. proposed that the softness of the inorganic lattice, which is closely associated with the small elastic coefficients, is an essential factor for the strong defect tolerance in halide perovskites.^[17,18] The lattice deformation induced by the defects immensely reduces the overlap between the free and trapped charges involved in the recombination, thus preventing the defects from acting as efficient non-radiative recombination centers.^[17,19] Therefore, investigating the elastic properties would also contribute to understanding the defect tolerance and seeking the lead-free halide double perovskites with high defect tolerance, which feature potential application in solar cells. Additionally, considering the structural design and performance optimization of devices, comprehensive knowledge of the elasticity is also essential because large thermo-mechanical stresses possibly occur in the device fabrication process, thus affecting the reliability of the devices.^[20] Nevertheless, a complete set of elastic coefficients has not yet been reported for this material. Similar to the lack of investigations for the elastic properties, although evaluating the lattice thermal conductivity matters for valuable insights into the fundamental phonon physics of this material and the stability of devices,^[21] few references about its lattice thermal conductivity have been reported. Hence, for the further progress of $\text{Cs}_2\text{Ag}_{1-x}\text{Na}_x\text{In}_{1-y}\text{Bi}_y\text{Cl}_6$ as white light-emitting material and X-Ray scintillators, a clear understanding of its elastic and thermal properties is necessary.

The techniques employed to determine the elasticity of materials include direct mechanical stress-strain methods,^[22] resonance ultrasonic spectroscopy (RUS),^[23] ultrasonic interferometry,^[24] and inelastic neutron scattering (INS).^[25] However, the requirement of large sample volumes hinders their applications in investigating the elasticity of low-dimensional materials. Unlike the listed techniques before, arising from the interaction of light with acoustic phonons close to the center of Brillouin zone (BZ) or spin waves in a medium, Brillouin light scattering (BLS) spectroscopy is a noncontact probe with a high spatial resolution of micrometer or even sub-micrometer defined by the size of laser beam focusing,^[26] which renders it a powerful and versatile tool to investigate the elastic properties for even

microscopic samples such as multilayered films^[27] and patterned nanostructures.^[28] Additionally, BLS measurements can also be conducted under high temperature in a furnace^[29] and high pressure in a diamond-anvil cell (DAC).^[30] The sound velocities attained from BLS measurements can help calculate the elastic coefficients and the lattice thermal conductivity (see Results and Discussion for details).

In this article, we reported on the first BLS study of the acoustic dynamics in $\text{Cs}_2\text{Ag}_{0.4}\text{Na}_{0.6}\text{InCl}_6:0.04\%\text{Bi}^{3+}$ and estimated the lattice thermal conductivity along the [111] direction via the experimentally average sound velocities. The measured Brillouin frequency shifts and thus the sound velocities of acoustic phonons were in good agreement with our first-principles calculations results of $\text{Cs}_2\text{Ag}_{0.5}\text{Na}_{0.5}\text{InCl}_6$. Using the angle-resolved Brillouin frequency shifts, all the three independent elastic coefficients for $\text{Cs}_2\text{Ag}_{0.4}\text{Na}_{0.6}\text{InCl}_6:0.04\%\text{Bi}^{3+}$ can be calculated. The elastic coefficients and lattice thermal conductivity we calculated here are significant for the understanding of STEs and for future researchers in designing devices like single-emitter-based white light-emitting devices and X-Ray scintillators which incorporate these new materials.

2. Basic Theory of BLS

The Brillouin spectra of $\text{Cs}_2\text{Ag}_{0.4}\text{Na}_{0.6}\text{InCl}_6:0.04\%\text{Bi}^{3+}$ were acquired using a confocal microscopic BLS system from JRS Scientific Instruments, which consists of a high-contrast (3 + 3)-pass tandem Fabry-Pérot (TFP-2 HC) interferometer and a confocal microscope (CM-1) with a 20× (numerical aperture [NA], 0.42) objective. **Figure 1** displays a schematic of our BLS setup. The beam from a 532 nm continuous-wave single-longitudinal mode laser was coupled into the microscope using a polarizing beam splitter (PBS), which almost entirely reflected the s-polarized light while nearly completely transmits the p-polarized component. The s-polarized component, if not analyzed, was then focused on the sample. Subsequently, the scattered radiation, collected and collimated by the same objective, was directed to and focused on the entrance pinhole of the interferometer to be frequency analyzed. Notably, two analyzers, namely a quarter-wave plate (QWP, $\lambda/4$) and a polarizer, can be utilized to obtain various polarization configurations, with only the QWP, both of them, and none of them in the beam path corresponding to circular polarization ($\sigma^+\sigma^-$), parallel polarization (VV), and perpendicular polarization (VH), respectively. In this article, V(H) refers to the polarization of light perpendicular (parallel) to the scattering plane. For example, VH represents the perpendicular (V) polarized incident light and parallel (H) polarized scattered light. To measure the angle-resolved BLS spectroscopy, a goniometer was incorporated in our experimental setup to alter the incident angle θ_i , as schematically shown in Figure 1.

The BLS of $\text{Cs}_2\text{Ag}_{0.4}\text{Na}_{0.6}\text{InCl}_6:0.04\%\text{Bi}^{3+}$ in our study arises from bulk acoustic waves (BAWs) but not surface acoustic waves.

J. Zhang
Beijing Academy of Quantum Information Science
Beijing 100193, China

P.-H. Tan, J. Zhang
CAS Center of Excellence in Topological Quantum Computation
University of Chinese Academy of Sciences
Beijing 100049, China

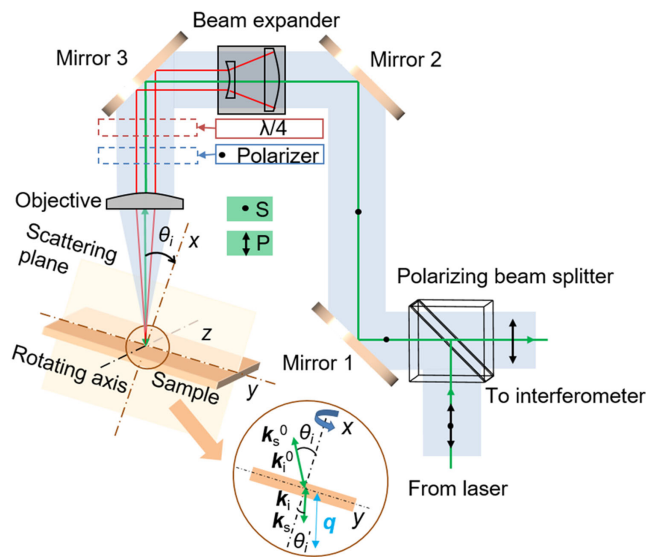


Figure 1. The schematic diagram of the Brillouin light scattering (BLS) setup highlighting the sketch of light and acoustic phonon wave vectors involved on the x - y plane. θ_i represents the incident angle outside the sample, while θ_i' denotes the refraction angle inside the sample. The green rectangles indicate the polarization directions of s - and p -polarized light, respectively.

For the direct scattering by a BAW, conservation of momentum and energy require that $\mathbf{k}_s = \mathbf{k}_i \pm \mathbf{q}$ and $hf_s = hf_i \pm hf$, where \mathbf{k}_i (f_i) and \mathbf{k}_s (f_s) are wave vectors (frequencies) of the incident and scattered light inside the sample, respectively. \mathbf{q} is the wave vector of acoustic phonon and f is the Brillouin frequency shift of the BAW. The \pm sign here accounts for a phonon being annihilated or created in the scattering process, namely the anti-Stokes and Stokes events, respectively. Based on the law of cosines, the magnitude of the wave vector \mathbf{q} of a BAW can be written as $q = \frac{4\pi n}{\lambda} \sin \frac{\varphi}{2}$, where n , λ , and φ are the refractive index, the wavelength of incident light (532 nm here), and the angle between the incident and scattered light, respectively. For the backscattering configuration ($\varphi = 180^\circ$) used in our study, the corresponding q

can be defined as $q = \frac{4\pi n}{\lambda}$. Within the long-wave limit, the acoustic branches exhibit linear dispersion and the sound velocity can be determined by $v = \frac{2\pi f}{q}$. See ref. [31] for a detailed derivation of the formulas mentioned before.

3. Results and Discussion

3.1. Structural Characterization

A truncated octahedral-shaped specimen of $\text{Cs}_2\text{Ag}_{0.4}\text{Na}_{0.6}\text{InCl}_6 \cdot 0.04\% \text{Bi}^{3+}$ crystal with a size of about $3 \times 3 \times 0.25 \text{ mm}^3$ (see the Experimental Section for more information about the sample preparation) was used for the BLS measurements. Since $\text{Cs}_2\text{NaInCl}_6$ and $\text{Cs}_2\text{AgInCl}_6$ possess the same structure and the lattice mismatch between them is as low as 0.30%, and the Na^+ incorporation into $\text{Cs}_2\text{AgInCl}_6$ would mainly randomly substitute Ag^+ at the M^+ sites, $\text{Cs}_2\text{Ag}_{0.4}\text{Na}_{0.6}\text{InCl}_6 \cdot 0.04\% \text{Bi}^{3+}$ can retain the original cubic structure of $\text{Cs}_2\text{AgInCl}_6$.^[11] In $\text{Cs}_2\text{AgInCl}_6$ whose space group is $Fm\bar{3}m$, the primitive unit cell contains 10 atoms, with one $[\text{AgCl}_6]$ and one $[\text{InCl}_6]$ octahedron alternating to form a rock-salt face-centered cubic (fcc) structure,^[13] while its conventional cubic unit cell contains 40 atoms. In our first-principles calculations, the crystal structure of $\text{Cs}_2\text{Ag}_{0.5}\text{Na}_{0.5}\text{InCl}_6$ we used is depicted in **Figure 2a**. As mentioned before, the actual structure of $\text{Cs}_2\text{Ag}_{0.5}\text{Na}_{0.5}\text{InCl}_6$ is Na^+ and Ag^+ mainly randomly occupying the M^+ sites. We used this layered structure (**Figure 2a**) as an approximation because it is a computationally more convenient structure for such a large doped supercell. The lattice constants of $\text{Cs}_2\text{Ag}_{0.5}\text{Na}_{0.5}\text{InCl}_6$ obtained from our first-principles calculations indicate merely a small contraction (0.4%) in the c direction. More details about the calculated lattice constants of $\text{Cs}_2\text{Ag}_{0.5}\text{Na}_{0.5}\text{InCl}_6$ are available in Experimental Section.

As shown in **Figure 2b**, X-Ray diffraction (XRD) pattern of the $\text{Cs}_2\text{Ag}_{0.4}\text{Na}_{0.6}\text{InCl}_6 \cdot 0.04\% \text{Bi}^{3+}$ crystal exhibits two strong diffraction peaks of (222) and (444) plane, and two weak peaks of (333) and (555) planes, which indicates that the sample is a single crystal and the sample surface we tested belongs to the (111) plane. It is worth noting that since the light sources used

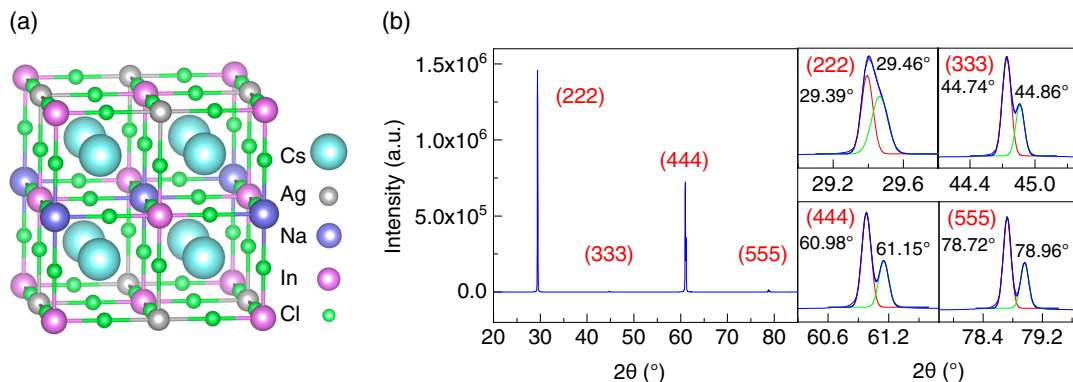


Figure 2. Crystal structure and the related structural characterization of $\text{Cs}_2\text{Ag}_{1-x}\text{Na}_x\text{In}_{1-y}\text{Bi}_y\text{Cl}_6$. a) Crystal structure of $\text{Cs}_2\text{Ag}_{0.5}\text{Na}_{0.5}\text{InCl}_6$ double perovskite used in the first-principles calculations. The mint green, gray, purple, fuchsia, and green spheres represent Cs, Ag, Na, In, and Cl atoms, respectively. b) X-Ray diffraction (XRD) patterns of $\text{Cs}_2\text{Ag}_{0.4}\text{Na}_{0.6}\text{InCl}_6 \cdot 0.04\% \text{Bi}^{3+}$ crystal. The right panels show the details of the (111) family of crystal planes obtained from the left panel.

in the XRD measurements are Cu $K\alpha_1$ and Cu $K\alpha_2$ ($\lambda_{K\alpha_1} = 1.540593 \text{ \AA}$, $\lambda_{K\alpha_2} = 1.544414 \text{ \AA}$), each crystallographic plane would correspond to two adjacent diffraction peaks, as shown in the right panels of Figure 2b. Moreover, the lattice constant ($a = 10.518 \text{ \AA}$) of $\text{Cs}_2\text{Ag}_{0.4}\text{Na}_{0.6}\text{InCl}_6:0.04\%\text{Bi}^{3+}$ can be calculated from the diffraction peaks.

3.2. First-Principles Calculations of Phonon Dispersion

We have calculated the phonon dispersion curves of $\text{Cs}_2\text{Ag}_{0.5}\text{Na}_{0.5}\text{InCl}_6$ including and excluding spin-orbit coupling (SOC), using the density-functional perturbation theory (DFPT)^[32] within the generalized gradient approximation (GGA).^[33] More details about the first-principles calculations are available in the Experimental Section. As shown in Figure 3a, the full phonon dispersion curves calculated without and with SOC have merely tiny frequency differences. To compare the frequency difference more intuitively, the frequency difference as a function of phonon frequency and wave vector is displayed in Figure 3b as a 3D colormap. As shown in Figure 3b, most of the phonon dispersion curves calculated including SOC deviate from the corresponding curves calculated excluding SOC within 0.5 cm^{-1} ($1 \text{ cm}^{-1} \approx 30 \text{ GHz}$), while the low-frequency optical branch closest to the longitudinal acoustic (LA) branch deviates within 2.6 cm^{-1} near the Γ point. And the LA branch deviates within 1.8 cm^{-1} at positions away from the Γ point, which suggests that the SOC would not have a great influence on the sound velocity of LA (the slope of the LA branch within the long-wave limit). In addition, the phonon dispersion of $\text{Cs}_2\text{Ag}_{0.5}\text{Na}_{0.5}\text{InCl}_6$ was also calculated using the DFPT within the Perdew–Zunger local density approximation (LDA)^[34] without considering SOC, as shown in Figure S1, Supporting Information. In Section 3.3, we would use the theoretical results corresponding to the GGA approach to further validate our assignment of the acoustic modes in $\text{Cs}_2\text{Ag}_{0.4}\text{Na}_{0.6}\text{InCl}_6:0.04\%\text{Bi}^{3+}$.

3.3. Assignment of the Acoustic Modes

In an anisotropic medium, when the acoustic phonon propagates parallel to a high-symmetry crystal axis, two pure transverse (T) and one longitudinal (L) acoustic waves are involved. In contrast,

for a general propagation direction, the involved acoustic modes are two quasi-transverse (QT) and one quasi-longitudinal (QL) ones.^[35] As discussed before, the sample surface examined is (111) crystallographic plane, thus the phonon wave vector direction was along [111] high-symmetry crystal axis when laser vertically impinged on the surface of the sample. Figure 4a shows a typical BLS spectrum of $\text{Cs}_2\text{Ag}_{0.4}\text{Na}_{0.6}\text{InCl}_6:0.04\%\text{Bi}^{3+}$ under VH polarization at $\theta_i = 0^\circ$. The (anti-)Stokes peaks were fit with Gaussian function to extract the Brillouin frequency shift (f). The BLS spectra under VH and VV polarization configurations with different incident angle (scattering angle) θ_i are displayed in Figure 4c,d, respectively. According to the Brillouin scattering polarization selection rules,^[36] the variation of peak intensity with polarization is helpful for the peak assignment. Under a given polarization configuration, the Brillouin scattered light intensity I is proportional to $[\hat{e}_s \cdot T \cdot \hat{e}_i]^2$, where \hat{e}_s and \hat{e}_i are unit vectors along the polarization direction of the scattered and incident light, respectively, and T is the Brillouin scattering tensor.^[36] Theoretically, at zero tilt, the intensity of T mode should dominate under cross-polarized (VH) condition while substantially decreasing under parallel-polarized (VV) configuration. As shown in Figure 4c,d, when $\theta_i = 0^\circ$, almost only the high-frequency peaks exist under VV polarization configuration, while the low-frequency ones with higher intensity appear under VH polarization configuration. Therefore, the high- and low-frequency peaks are most likely attributed to longitudinal (L) and transverse (T) acoustic modes, respectively. Meanwhile, this assignment satisfies the condition that the frequency of L mode is generally higher than that of T mode. To further confirm the assignment of the acoustic modes, we compared the frequencies of acoustic phonons calculated using the GGA method including SOC with our experimental results. The acoustic branches near the Γ point with the path of $A-\Gamma-X-R-\Gamma$ (extracted from the phonon dispersion of $\text{Cs}_2\text{Ag}_{0.5}\text{Na}_{0.5}\text{InCl}_6$ calculated using the GGA method with SOC, as shown in the right panel of Figure 3a), which exhibit linear dispersion, are shown in Figure 4b. The experimentally average Brillouin frequency shifts (11.52 and 21.04 GHz) are denoted by the symbols in Figure 4b, which were extracted by averaging the frequency values of 10 randomly selected positions on the sample under VH polarization configuration when $\theta_i = 0^\circ$. As exhibited in Figure 4b, our experimentally average Brillouin frequency shifts are well consistent

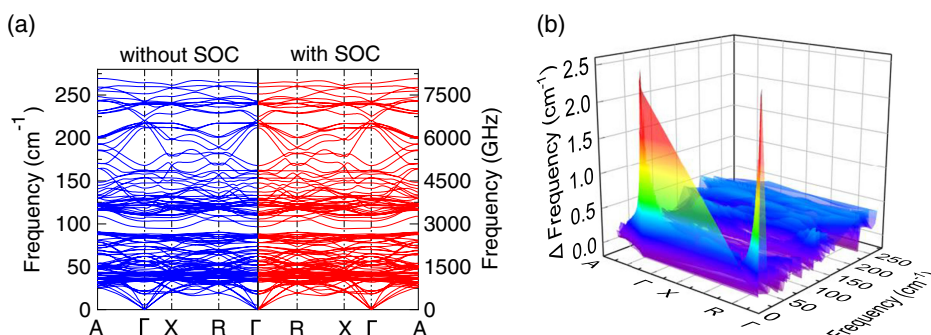


Figure 3. Phonon dispersions of $\text{Cs}_2\text{Ag}_{0.5}\text{Na}_{0.5}\text{InCl}_6$ calculated using the generalized gradient approximation (GGA) method. a) Full phonon dispersion curves of $\text{Cs}_2\text{Ag}_{0.5}\text{Na}_{0.5}\text{InCl}_6$ calculated without and with spin-orbit coupling (SOC). b) Frequency difference ($\Delta \text{ Frequency} = \text{Frequency} [\text{without SOC}] - \text{Frequency} [\text{with SOC}]$) as a function of frequency and wave vector of phonons, obtained from (a).

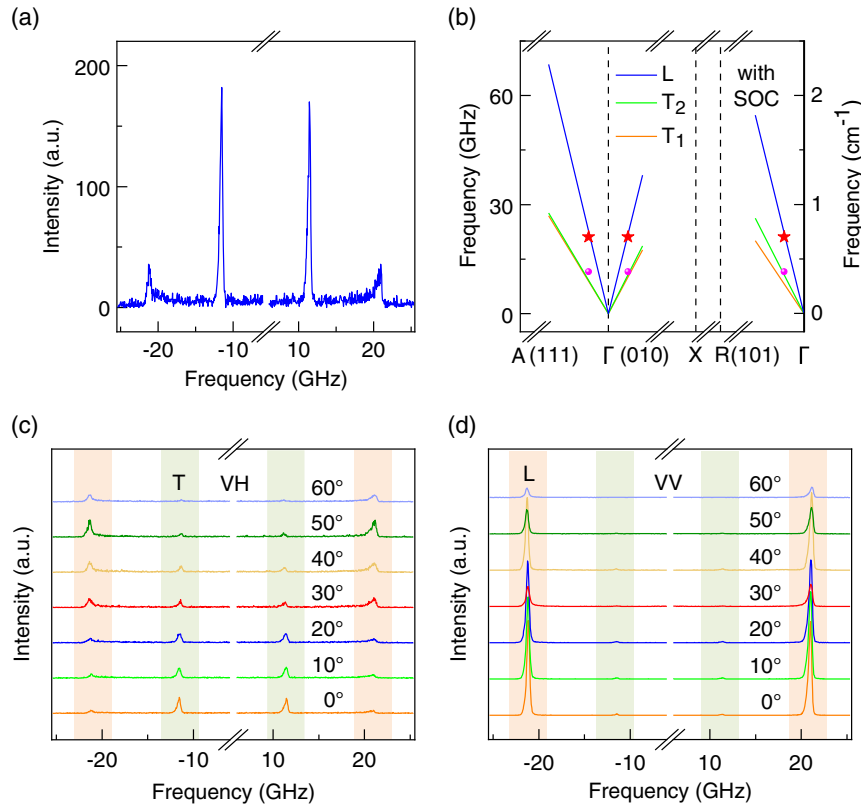


Figure 4. Experimental BLS frequencies and the calculated acoustic phonon dispersion of $\text{Cs}_2\text{Ag}_{1-x}\text{Na}_x\text{In}_{1-y}\text{Bi}_y\text{Cl}_6$. a) A representative BLS spectrum of $\text{Cs}_2\text{Ag}_{0.4}\text{Na}_{0.6}\text{InCl}_6:0.04\%\text{Bi}^{3+}$ under VH polarization configuration when $\theta_i = 0^\circ$. b) Part of the calculated acoustic phonon dispersion (including SOC) along the path of $\text{A}-\Gamma-\text{X}-\text{R}-\Gamma$. The L , T_2 , and T_1 modes are denoted by solid lines with different colors while the symbols correspond to the experimentally average Brillouin frequency shifts (11.52 and 21.04 GHz), which were extracted by averaging the frequency values of 10 randomly selected positions on the sample under VH polarization configuration when $\theta_i = 0^\circ$. The BLS spectra under c) VH and d) VV polarization configurations with different scattering angle θ_i . The T modes are marked with the green background while the L modes are marked with the orange one.

with the results of the first-principles calculations (solid lines), which further verifies our assignment of the acoustic modes.

Combining the measured frequencies of acoustic modes and $v = \frac{2\pi f}{q}$, we can obtain the corresponding sound velocities. To calculate the magnitude of scattered phonon wave vector q , the refractive index of the sample is required according to the formula $q = \frac{4\pi n}{\lambda}$. The refractive index here was estimated based on linear interpolation^[37] using $n_{\text{Cs}_2\text{Ag}_{0.4}\text{Na}_{0.6}\text{InCl}_6} = 0.4n_{\text{Cs}_2\text{AgInCl}_6} + 0.6n_{\text{Cs}_2\text{NaInCl}_6}$, where the refractive indices of $\text{Cs}_2\text{AgInCl}_6$ (mp-1096 926) and $\text{Cs}_2\text{NaInCl}_6$ (mp-989 571) obtained from Materials Project database are 1.89 and 1.68, respectively.^[38,39] Therefore, the refractive index for $\text{Cs}_2\text{Ag}_{0.4}\text{Na}_{0.6}\text{InCl}_6$ is 1.76, yielding $q = 4.16 \times 10^5 \text{ cm}^{-1}$. Theoretically, the Bi^{3+} doping would increase the refractive index.^[40,41] However, since just a small amount of Bi^{3+} was doped, we expected that it would have negligible influence on the refractive index of the sample and it is reasonable to consider that $\text{Cs}_2\text{Ag}_{0.4}\text{Na}_{0.6}\text{InCl}_6:0.04\%\text{Bi}^{3+}$ possesses the same refractive index as $\text{Cs}_2\text{Ag}_{0.4}\text{Na}_{0.6}\text{InCl}_6$. The experimental frequencies and calculated velocities of acoustic phonons in $\text{Cs}_2\text{Ag}_{0.4}\text{Na}_{0.6}\text{InCl}_6:0.04\%\text{Bi}^{3+}$ as a function of $\sin\theta_i$ under VH (T modes) and VV (L modes) polarization

configurations are shown in **Figure 5c,d**, respectively. Because the sound velocity is proportional to the Brillouin frequency shift, they display the same trend with $\sin\theta_i$. Next, we would fit the velocity as a function of $\sin\theta_i$, as shown in the solid lines in **Figure 5c,d**, respectively.

Considering the sound velocity of a BAW propagating along an arbitrary direction, Xie et al. proposed a resultant method to calculate the sound velocity by establishing the connection between the sound velocities of the acoustic phonons propagating along the high-symmetry axes in the first BZ and the phonon wave vector involved in the scattering,^[42] which can also be applied to our work. For a given Bravais lattice, the first BZ and the corresponding irreducible wedge (IW) can be figured out. Since the $\text{Cs}_2\text{Ag}_{0.4}\text{Na}_{0.6}\text{InCl}_6:0.04\%\text{Bi}^{3+}$ we examined belongs to the fcc structure, we plotted the IW for BZ in **Figure 5a**. The letters label high-symmetry points and axes. As mentioned before, the propagation direction of the acoustic phonon we investigated is along the high-symmetry crystal axis [111] (ΓL) when $\theta_i = 0^\circ$. While rotating, the propagation direction of the acoustic phonon (ΓB in **Figure 5b**) would tilt away from the [111] direction by an amount dictated by Snell's law, that is, the phonon wave vector would vary from the ΓL to ΓX direction in the ΓLUX plane of the IW, as indicated in **Figure 5b**.

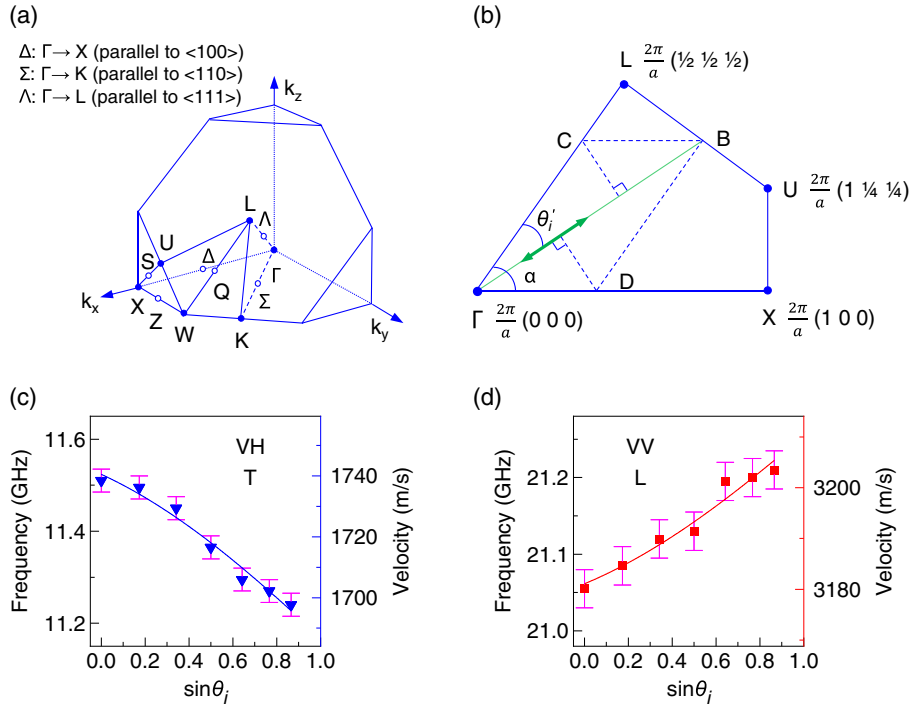


Figure 5. The schematic diagrams of BZ for fcc lattice, together with the experimental BLS frequencies and the related sound velocities of $\text{Cs}_2\text{Ag}_{0.4}\text{Na}_{0.6}\text{InCl}_6:0.04\%\text{Bi}^{3+}$. a) The $1/8$ of the first BZ and the iBZ for the BZ of fcc lattice. Letters label symmetry points and axes. b) The ΓLUX plane obtained from (a). θ_i denotes the refraction angle inside the sample. The green double arrow corresponds to the wave vector of a BAW. The blue dotted lines and the green solid one are the auxiliary lines. The experimental frequency extracted from the average value of Stokes and anti-Stokes frequencies, and the calculated velocity of $\text{Cs}_2\text{Ag}_{0.4}\text{Na}_{0.6}\text{InCl}_6:0.04\%\text{Bi}^{3+}$ as a function of $\sin\theta_i$ under c) perpendicular polarization (VH) (T modes) and d) parallel polarization (VV) (L modes) configurations. The solid symbols correspond to the experimental results. The error bars represent the spectral resolution (0.05 GHz) and the velocity resolution (8 m s^{-1}). The solid lines are the fitting curves of sound velocity based on Equation (2).

Utilizing the resultant method mentioned by Xie et al.,^[42] the velocity ($v_{\Gamma\text{B}}$) of a BAW traveling along an arbitrary direction between the ΓL and ΓX direction can be written as the combination of the velocities corresponding to the ΓL ($v_{\Gamma\text{L}}$) and ΓX ($v_{\Gamma\text{X}}$) directions.

$$qv_{\Gamma\text{B}} = q_{\Gamma\text{L}}v_{\Gamma\text{L}} \cos \theta'_i + q_{\Gamma\text{X}}v_{\Gamma\text{X}} \cos(\alpha - \theta'_i) \quad (1)$$

where α is the angle between the ΓL and ΓX direction, and θ'_i represents the refraction angle inside the sample. Combining Snell's law and the geometrical relationship shown in Figure 5b, Equation (1) can be rewritten as

$$v_{\Gamma\text{B}} = \frac{\cos\alpha}{\sin\alpha} (v_{\Gamma\text{X}} - v_{\Gamma\text{L}}) \frac{n_0 \sin \theta_i \sqrt{n^2 - n_0^2 \sin^2 \theta_i}}{n^2} + v_{\Gamma\text{L}} \frac{n^2 - n_0^2 \sin^2 \theta_i}{n^2} + v_{\Gamma\text{X}} \frac{n_0^2 \sin^2 \theta_i}{n^2} \quad (2)$$

where $n_0 = 1$ is the refractive index of air, and θ_i denotes the incident angle (scattering angle) outside the sample. $\frac{\cos\alpha}{\sin\alpha}$ can be calculated to be $\frac{\sqrt{2}}{2}$ here. According to Equation (2), we can fit the velocity $v_{\Gamma\text{B}}$ as a function of $\sin\theta_i$, as shown in the solid lines in Figure 5c,d, which are in good accordance with the experimental results (solid symbols in Figure 5c,d). The fitting variables are listed as follows: for the T modes (Figure 5c), $v_{\Gamma\text{L}}^{\text{T}} = 1740$,

and $v_{\Gamma\text{X}}^{\text{T}} = 1658 \text{ m s}^{-1}$, while for the L modes (Figure 5d), $v_{\Gamma\text{L}}^{\text{L}} = 3181$, and $v_{\Gamma\text{X}}^{\text{L}} = 3226 \text{ m s}^{-1}$, which have been tabulated in column five of Table 1. Furthermore, as listed in column four of Table 1, for $\text{Cs}_2\text{Ag}_{0.4}\text{Na}_{0.6}\text{InCl}_6:0.04\%\text{Bi}^{3+}$, the sound velocities of the acoustic phonons travelling along [111] direction were calculated using the experimentally average Brillouin frequency shifts (11.52 and 21.04 GHz, as indicated in Figure 4b). From Table 1, we can find that the fitting sound velocities of the acoustic phonons propagating along [111] direction and the ones obtained from the experimental Brillouin frequency shifts agree well with each other.

3.4. Analysis of the Elastic Coefficients

The measurement of Brillouin frequency shift enables the calculations of the velocity of acoustic waves thus the elastic coefficients of crystals. Based on the expansion of Christoffel's equation, the elastic coefficients of a given crystal are intrinsically coupled with one another. The basic calculation process can be found in the Experimental Section. In the cubic system with space group $Fm\bar{3}m$, the corresponding sound velocities of different acoustic modes for different directions are tabulated in column three of Table 1. The velocity is given by $v = \sqrt{X/\rho}$ ^[35], where X is an appropriate combination of the elastic coefficients (C_{ij}). For the cubic $\text{Cs}_2\text{Ag}_{0.4}\text{Na}_{0.6}\text{InCl}_6:0.04\%\text{Bi}^{3+}$, only three

Table 1. The sound velocities of different acoustic modes propagating along various directions in Cs₂Ag_{0.4}Na_{0.6}InCl₆:0.04%B³⁺ (space group *Fm* $\bar{3}$ *m*).

Propagation direction of q	Acoustic mode	Sound velocity $v = \sqrt{X/\rho}$ ^[35]	Sound velocity value [m s ⁻¹]	
<100> ($\Gamma \rightarrow X$)	v_{T_1}	$\sqrt{C_{44}/\rho}$	1658 ^{b)}	
	v_{T_2}	$\sqrt{C_{44}/\rho}$	1658 ^{b)}	
	v_L	$\sqrt{C_{11}/\rho}$	3226 ^{b)}	
<110> ($\Gamma \rightarrow K$)	v_{T_1}	$\sqrt{(C_{11} - C_{12})/2\rho}$		
	v_{T_2}	$\sqrt{C_{44}/\rho}$		
	v_L	$\sqrt{(C_{11} + C_{12} + 2C_{44})/2\rho}$		
<111> ($\Gamma \rightarrow L$)	v_{T_1}	$\sqrt{(C_{11} - C_{12} + C_{44})/3\rho}$	1740 ^{a)}	1740 ^{b)}
	v_{T_2}	$\sqrt{(C_{11} - C_{12} + C_{44})/3\rho}$	1740 ^{a)}	1740 ^{b)}
	v_L	$\sqrt{(C_{11} + 2C_{12} + 4C_{44})/3\rho}$	3178 ^{a)}	3181 ^{b)}

^{a)}Corresponds to the calculated results using the experimentally average Brillouin frequency shifts (11.52 and 21.04 GHz, as indicated in Figure 4b); ^{b)}Corresponds to the fitting results of the velocity as a function of $\sin\theta$, under perpendicular polarization (VH) and parallel polarization (VV) configurations (Figure 5c,d) using Equation (2).

independent C_{ij} (C_{11} , C_{12} , and C_{44}) elements exist. The mass density $\rho = 3.712 \text{ g cm}^{-3}$ of Cs₂Ag_{0.4}Na_{0.6}InCl₆:0.04%B³⁺ was calculated from the lattice constant ($a = 10.518 \text{ \AA}$) and the molecular weight M (using the molecular weight of Cs₂Ag_{0.4}Na_{0.6}InCl₆ as an approximation), according to the formula $\rho = N \cdot M / (N_A \cdot V)$. Here, N is the number of motifs per unit cell. V is the volume of the unit cell ($V = a^3$), and N_A is Avogadro's number.

As shown in Table 1, based on the sound velocities of the acoustic phonons propagating along [100] direction, C_{44} and C_{11} for the experimental sample Cs₂Ag_{0.4}Na_{0.6}InCl₆:0.04%B³⁺ can be calculated as 10.20 and 38.63 GPa, respectively. Additionally, using the values of C_{44} and C_{11} , together with the velocities of the acoustic phonons with q traveling along [111] direction, the remaining independent elastic coefficient (C_{12}) can be calculated as 16.11 GPa. The complete set of elastic coefficients derived from the sound velocities is listed in line two of Table 2. All of the calculated elastic constants in this work are positive, satisfying the Born stability criteria for a cubic system:^[43] $C_{11} + 2C_{12} > 0$, $C_{11} > |C_{12}|$, and $C_{44} > 0$. For the first-principles-calculated specimen Cs₂Ag_{0.5}Na_{0.5}InCl₆, the corresponding sound velocities and elastic coefficients are displayed in Table S1 and S2, Supporting Information, respectively. As shown in columns six and seven of Table 2, we also calculated the bulk modulus Voigt–Reuss–Hill (VRH) average K_{VRH} and shear modulus VRH average G_{VRH} of Cs₂Ag_{0.4}Na_{0.6}InCl₆:0.04%B³⁺. The calculation details are presented in the Experimental Section. Moreover, the theoretical elastic quantities of some other halide double perovskites obtained from previous reports and the Materials Project database are also shown in Table 2 for comparison. The K_{VRH} and

Table 2. Elastic coefficients and related elastic quantities of halide double perovskites in units of GPa.

Material		C_{11}	C_{12}	C_{44}	K_{VRH}	G_{VRH}
Cs ₂ Ag _{0.4} Na _{0.6} InCl ₆ :0.04%B ³⁺	This work	38.63	16.11	10.20	23.62	10.61
Cs ₂ AgInCl ₆ ^{a)}	[46]	93.03	23.69	15.91	46.80	21.86
Cs ₂ AgInCl ₆ ^{b)}	[39]				30.49	8.71
Cs ₂ NaInCl ₆ ^{a)}	[41]	243.27	119.73	87.14	160.91	75.91
Cs ₂ NaInCl ₆ ^{b)}	[39]				28.31	8.99
Cs ₂ NaSbCl ₆ ^{a)}	[41]	259.03	126.21	91.20	170.84	80.31
Cs ₂ NaSbCl ₆ ^{b)}	[39]	32	13	11	20	11
Cs ₂ NaTiCl ₆ ^{a)}	[41]	315.49	109.32	97.76	174.71	97.88
Cs ₂ NaTiCl ₆ ^{b)}	[39]				26.36	8.11
Cs ₂ NaBiCl ₆ ^{a)}	[41]	316.62	113.22	76.18	181.02	85.52
Cs ₂ NaBiCl ₆ ^{b)}	[39]				25.41	7.92
Cs ₂ AgBiCl ₆ ^{a)}	[47]	69.01	16.51	10.63	34.01	15.41
Cs ₂ AgBiCl ₆ ^{b)}	[39]				27.42	7.76
Cs ₂ AgBiBr ₆ ^{a)}	[47]	67.60	8.76	6.59	28.37	12.64
Cs ₂ AgBiBr ₆ ^{b)}	[39]				22.40	7.48

^{a)}Corresponds to the theoretical results reported in previous papers; ^{b)}Corresponds to the theoretical results obtained from the Materials Project database.

G_{VRH} obtained from the Materials Project database were predicted using the statistical learning (SL) models,^[39,44] while the elastic coefficients of Cs₂NaSbCl₆ obtained from the Materials Project database were calculated using the strain–stress method.^[39,45] As can be seen in Table 2, the K_{VRH} (G_{VRH}) obtained from the Materials Project database for different halide double perovskites including Cs₂AgInCl₆ and Cs₂NaInCl₆ are in the range of 20–31 GPa (7–11 GPa), which can further validate our calculated results for Cs₂Ag_{0.4}Na_{0.6}InCl₆:0.04%B³⁺ since the K_{VRH} (G_{VRH}) of Cs₂Ag_{0.4}Na_{0.6}InCl₆:0.04%B³⁺ is 23.62 GPa (10.61 GPa). In contrast, the elastic coefficients reported by Haque and Hossain^[46,47] and Khan et al.^[41] were overestimated, especially the data provided by Khan et al.^[41] We can find from Table 2 that the elasticity of Cs₂Ag_{0.4}Na_{0.6}InCl₆:0.04%B³⁺ is low, which manifests a soft lattice, similar to some other halide double perovskites.

3.5. Estimate of the Lattice Thermal Conductivity

Employing the velocities of the acoustic phonons propagating along the [111] direction we examined, the lattice thermal conductivity (κ_L) can be estimated based on the framework of Slack's equation^[48]: $\kappa_L = A \frac{M_a \delta_s^{1/3} \theta_d^3}{\gamma^2 T}$, where M_a , δ^3 , s , θ_d , γ , and A are the average atomic mass, volume per atom, number of atoms in the primitive unit cell, acoustic Debye temperature, acoustic Grüneisen parameter, and $A = \frac{2.43 \times 10^{-8}}{1 - 0.514/\gamma + 0.228/\gamma^2}$ ^[49] respectively. It is worth noting that the M_a and s here were attained from Cs₂Ag_{0.4}Na_{0.6}InCl₆, neglecting the influence of the 0.04%B³⁺ incorporation. According to the formulas indicated in the Experimental Section, we estimated the room-temperature lattice thermal conductivity and the related thermal

Table 3. Lattice thermal conductivity and related thermal quantities along the [111] direction of $\text{Cs}_2\text{Ag}_{0.4}\text{Na}_{0.6}\text{InCl}_6:0.04\%\text{Bi}^{3+}$.

Acoustic mode	Sound velocity v [m s^{-1}] ^{a)}	Acoustic Debye temperature θ_a [K]	Poisson ratio ν	Acoustic Grüneisen parameter γ	Lattice thermal conductivity κ_L [$\text{W m}^{-1} \text{K}^{-1}$]
T	1740				
L	3178	87	0.29	1.71	1.03

^{a)}The sound velocities were obtained from the experimentally average values in Table 1, related to the acoustic phonons propagating along the [111] direction.

quantities along the [111] direction of $\text{Cs}_2\text{Ag}_{0.4}\text{Na}_{0.6}\text{InCl}_6:0.04\%\text{Bi}^{3+}$, as tabulated in Table 3. The low acoustic Debye temperature (merely 87 K) of $\text{Cs}_2\text{Ag}_{0.4}\text{Na}_{0.6}\text{InCl}_6:0.04\%\text{Bi}^{3+}$ reveals the weak interatomic potential, which normally indicates that the crystal structure can be easily deformed under mechanical stress,^[50,51] leading to the weak elastic properties, as discussed in the former section. It is reported that the crystals with a room-temperature value of κ_L smaller than $100 \text{ W m}^{-1} \text{K}^{-1}$ are considered to possess a low lattice thermal conductivity.^[50] A very low κ_L along the [111] direction of $\text{Cs}_2\text{Ag}_{0.4}\text{Na}_{0.6}\text{InCl}_6:0.04\%\text{Bi}^{3+}$, approximately $1.03 \text{ W m}^{-1} \text{K}^{-1}$, similar to many compounds with rock-salt structure, is potentially due to its strong lattice anharmonicity.^[50,51] It is worth noting that the κ_L of $\text{Cs}_2\text{Ag}_{0.4}\text{Na}_{0.6}\text{InCl}_6:0.04\%\text{Bi}^{3+}$ we calculated here is an estimate, thus further precise determination of the lattice thermal conductivity using the experimental methods is required. Nevertheless, estimating the value of lattice thermal conductivity based on the framework of Slack's equation is reasonable and the value of κ_L we calculated here would probably still be in the same order of magnitudes as the actual κ_L , which can yet reflect the characteristic of very low κ_L in the halide double perovskite $\text{Cs}_2\text{Ag}_{0.4}\text{Na}_{0.6}\text{InCl}_6:0.04\%\text{Bi}^{3+}$.

4. Conclusion

In summary, angle-resolved Brillouin light scattering measurements were firstly performed for a bulk doped halide double perovskite $\text{Cs}_2\text{Ag}_{0.4}\text{Na}_{0.6}\text{InCl}_6:0.04\%\text{Bi}^{3+}$ crystal. The high-(low)-frequency modes observed were identified to the longitudinal (transverse) bulk acoustic modes propagating along the [111] direction. The measured Brillouin frequency shifts of $\text{Cs}_2\text{Ag}_{0.4}\text{Na}_{0.6}\text{InCl}_6:0.04\%\text{Bi}^{3+}$ agrees with the first-principles calculated dispersion of $\text{Cs}_2\text{Ag}_{0.5}\text{Na}_{0.5}\text{InCl}_6$. By exploiting the relationship between the Brillouin frequency shifts, the sound velocities, and the elastic coefficients, a complete set of elastic coefficients and other elastic quantities for $\text{Cs}_2\text{Ag}_{0.4}\text{Na}_{0.6}\text{InCl}_6:0.04\%\text{Bi}^{3+}$ were calculated: $C_{11} = 38.63$, $C_{12} = 16.11$, $C_{44} = 10.20$, $K_{\text{VRH}} = 23.62$, and $G_{\text{VRH}} = 10.61 \text{ GPa}$. The low elasticity would contribute to our understanding of the STEs formation in $\text{Cs}_2\text{Ag}_{1-x}\text{Na}_x\text{In}_{1-y}\text{Bi}_y\text{Cl}_6$. Furthermore, utilizing the Brillouin frequency shifts observed, the $\text{Cs}_2\text{Ag}_{0.4}\text{Na}_{0.6}\text{InCl}_6:0.04\%\text{Bi}^{3+}$ crystal was found to exhibit an ultralow acoustic Debye temperature (87 K) and lattice thermal conductivity ($1.03 \text{ W m}^{-1} \text{K}^{-1}$) along the [111] direction, reflecting its weak interatomic potential and strong anharmonicity,

respectively. Our results provide elastic and thermal properties of $\text{Cs}_2\text{Ag}_{0.4}\text{Na}_{0.6}\text{InCl}_6:0.04\%\text{Bi}^{3+}$ and we expected that these results would facilitate research for $\text{Cs}_2\text{Ag}_{1-x}\text{Na}_x\text{In}_{1-y}\text{Bi}_y\text{Cl}_6$ on single-emitter-based white light-emitting phosphors and diodes for next-generation lighting and display technologies. In addition, our approach to investigate the elastic and thermal properties using angle-resolved BLS spectroscopy is also applicable to other materials with different crystal structures.

5. Experimental Section

Sample Preparation: $\text{Cs}_2\text{Ag}_{0.4}\text{Na}_{0.6}\text{InCl}_6:0.04\%\text{Bi}^{3+}$ crystal was synthesized by a hydrothermal method, in which the CsCl , AgCl , NaCl , InCl_3 , and BiCl_3 precursors were mixed into a concentrated HCl solution in a hydrothermal autoclave, being heated for a given time and then slowly cooled down. The Bi^{3+} doping into the sample was a small amount (merely 0.04%, atomic ratio to In). Further details on sample preparation can be found elsewhere.^[11]

BLS Measurements: Concerning the BLS spectroscopic measurement details, the spectral resolution was 0.05 GHz, with contrast larger than 150 dB. Laser power impinging on the sample was 2 mW, and the typical acquisition time was about 25 min per spectrum. All measurements were carried out at room temperature using 180° backscattering geometry. Additionally, with the goniometer incorporated in our experimental setup, the incident angle θ_i could be changed systematically and precisely (The angle accuracy is $<1^\circ$). The sample was tilted by an angle θ_i ranging from 0° to 60° in our angle-resolved BLS measurements.

Calculations of Direction-Dependent Sound Velocities: Utilizing the resultant method, we obtained the velocities of the acoustic phonons traveling along $\langle 100 \rangle$ and $\langle 111 \rangle$ directions, as mentioned in Section 3.3. It is worth noting that Xie et al.^[42] stated that if $v_{\Gamma\text{U}}$ was significantly different from $v_{\Gamma\text{X}}$, the existence of the ΓU path (Figure 5b) would lead the $v_{\Gamma\text{X}}$ in Equation (2) to change with θ_i ($v_{\Gamma\text{X}} = v_0 + \beta \sin\theta_i$), where v_0 is the value of $v_{\Gamma\text{X}}$ when $\theta_i = 0^\circ$ and β is a θ_i -dependent parameter due to the contribution of $v_{\Gamma\text{U}}$. However, the fitting errors for the variables were relatively larger when including the contribution of the $v_{\Gamma\text{U}}$, compared with the fitting results without considering the contribution of the $v_{\Gamma\text{U}}$, which thus have been displayed in Figure 5c,d, respectively.

Theoretically, for any given crystal structure, a degeneracy in two transverse mode frequencies occurs if the axis of symmetry where the acoustic phonon propagates along is of a higher order than two.^[52] Thus, in the case of our sample as a cubic crystal, the two transverse modes propagating along $\langle 100 \rangle$ (ΓX , a fourfold axis) and $\langle 111 \rangle$ (ΓL , a threefold axis) directions should be degenerated and hold the identical velocities, respectively, while the v_{Γ_1} and v_{Γ_2} corresponding to the $\langle 110 \rangle$ (ΓK) direction differ from each other, as shown in column three of Table 1. Therefore, if the phonon wave vector we detected varied from the ΓL to ΓK direction while rotating the sample, the degenerate transverse mode would split into two transverse modes with different velocities. However, as shown in Figure 5c, only one transverse mode appeared when changing the scattering angle θ_i in our measurements, we could thus conclude that the phonon wave vector tilted away from the ΓL to ΓX direction, but not the ΓK direction, as discussed in Section 3.3.

Calculations of Elastic Coefficients and Related Elastic Quantities: Based on the BLS-measured direction-dependent sound velocities, the elastic coefficients of a given crystal could be obtained within the framework of the Christoffel's equation: nontrivial solutions, corresponding to the velocities of three acoustic modes in the vicinity of the BZ center, are obtained by setting the characteristic determinant of the Christoffel equation for an anisotropic solid as zero.^[52,53]

$$|C_{ijkl}q_jq_k - \rho v^2\delta_{il}| = 0 \quad (3)$$

where C_{ijkl} are the components of the elastic stiffness tensor, q_j , q_k are the direction cosines of the unit vector normal to the wave plane, ρ is the

density of the material, and δ_{ij} is the Kronecker delta function. By connecting the elastic coefficients, Equation (3) could be rewritten as^[52]

$$\begin{vmatrix} \lambda_{11} - \rho v^2 & \lambda_{12} & \lambda_{13} \\ \lambda_{12} & \lambda_{22} - \rho v^2 & \lambda_{23} \\ \lambda_{13} & \lambda_{23} & \lambda_{33} - \rho v^2 \end{vmatrix} = 0 \quad (4)$$

where the λ_{ij} elements are the combination of direction cosines and C_{ij} elements. Detailed descriptions and formulae about λ_{ij} are provided by Auld.^[52]

In the case of cubic crystals containing three independent C_{ij} (C_{11} , C_{12} , and C_{44}) elements, the elastic stiffness tensor is subject to the following form.^[52]

$$\begin{pmatrix} C_{11} & C_{12} & C_{12} & 0 & 0 & 0 \\ C_{12} & C_{11} & C_{12} & 0 & 0 & 0 \\ C_{12} & C_{12} & C_{11} & 0 & 0 & 0 \\ 0 & 0 & 0 & C_{44} & 0 & 0 \\ 0 & 0 & 0 & 0 & C_{44} & 0 \\ 0 & 0 & 0 & 0 & 0 & C_{44} \end{pmatrix} \quad (5)$$

Hence, the corresponding λ_{ij} elements could be reduced to the following simple form.^[52]

$$\begin{aligned} \lambda_{11} &= q_x^2 C_{11} + q_y^2 C_{44} + q_z^2 C_{44} \\ \lambda_{22} &= q_x^2 C_{44} + q_y^2 C_{11} + q_z^2 C_{44} \\ \lambda_{33} &= q_x^2 C_{44} + q_y^2 C_{44} + q_z^2 C_{11} \\ \lambda_{12} &= q_x q_y (C_{12} + C_{44}) \\ \lambda_{23} &= q_y q_z (C_{12} + C_{44}) \\ \lambda_{13} &= q_x q_z (C_{12} + C_{44}) \end{aligned} \quad (6)$$

Therefore, if the elastic coefficients C_{ij} of the cubic crystals are available, the three sound velocities v_i for an arbitrary direction (q_x, q_y, q_z) phonon propagating along could be easily calculated using Equation (4) and (6). In contrast, it is theoretically possible to derive full elastic tensors of a given crystal by measuring velocities in a sufficient number of arbitrary directions. Particularly, by judiciously selecting the directions of measurement, like the high-symmetry directions ([100], [110], together with [111] directions in cubic system, and others), the algebra could be considerably simplified.

Additionally, for the cubic structure, the bulk (shear) modulus Voigt average [K_V (G_V)], which is the upper bound on K (G) for polycrystalline material, and the bulk (shear) modulus Reuss average [K_R (G_R)] representing the lower bound on K (G) could be described as^[45,54] $K_R = K_V = \frac{C_{11} + 2C_{12}}{3}$, $G_V = \frac{C_{11} - C_{12} + 3C_{44}}{5}$, and $G_R = \frac{5C_{44}(C_{11} - C_{12})}{4C_{44} + 3(C_{11} - C_{12})}$, respectively. K_{VRH} is the average of K_V and K_R , while G_{VRH} is the average of G_V and G_R .

Estimate of Lattice Thermal Conductivity and Related Thermal Quantities: As mentioned in Section 3.5, to evaluate the value of κ_L , it was necessary to obtain the values of θ_a and γ first. Acoustic Debye temperature θ_a could be expressed using the average velocity v_a ^[51]: $\theta_a = \frac{h}{k_B} \left(\frac{3m}{4\pi} \right)^{1/3} v_a s^{-1/3}$, where h , k_B , and m are the Planck constant, Boltzmann constant, and the number of atoms per volume, respectively. v_a is a combination of longitudinal (v_L) and transverse (v_S) sound velocity. For $\text{Cs}_2\text{Ag}_{0.4}\text{Na}_{0.6}\text{InCl}_6:0.04\%\text{Bi}^{3+}$ with the (111) surface we examined, the average sound velocity along [111] direction could be described as^[55] $v_a = \left[\frac{1}{3} \left(\frac{2}{v_S^3} + \frac{1}{v_L^3} \right) \right]^{-1/3}$. In addition, the relationship between the Poisson ratio ν and the Grüneisen parameter γ could be expressed as^[56,57] $\nu = \frac{1 - 2(v_S/v_L)^2}{2 - 2(v_S/v_L)^2}$ and $\gamma = \frac{3}{2} \left(\frac{1 + \nu}{2 - 3\nu} \right)$, respectively. Since these two formulas are valid for the materials with the rock-salt structure,^[51] they could be exploited to estimate the γ of $\text{Cs}_2\text{Ag}_{0.4}\text{Na}_{0.6}\text{InCl}_6:0.04\%\text{Bi}^{3+}$.

XRD Measurements: Structural identification of the sample was carried out using a Rigaku SmartLab diffractometer with Cu $K\alpha$ radiation ($\lambda_{K\alpha_1} = 1.540593$, $\lambda_{K\alpha_2} = 1.544414$ Å). The $\theta/2\theta$ scan, ω (incident angle between

the X-Ray source and the sample) scan, χ (tilt angle from sample surface normal direction) scan, φ (rotation angel around sample surface normal direction) scan, and $2\theta/\omega$ scan were performed for the sample to index the plane parallel to the sample surface, as shown in Figure 2b, where only the diffraction peaks correspond to the (111) family of crystal planes appeared. The optimized parameters we obtained here were $\chi = -1.3^\circ$ and $\varphi = -0.3^\circ$.

First-Principles Calculations: All calculations on $\text{Cs}_2\text{Ag}_{0.5}\text{Na}_{0.5}\text{InCl}_6$ were performed using the first-principles method with the Optimized Norm-Conserving Vanderbilt Pseudopotentials^[58] as implemented in QUANTUM ESPRESSO package.^[59] The GGA^[33] was adopted to describe the exchange–correlation potential. The phonon dispersion was calculated using the DFPT with and without considering SOC.^[32] We used a single Γ point with a plane-wave energy cutoff of 100 Ry and the atomic positions were relaxed until the Hellmann–Feynman forces on each atom became less than 10^{-5} Ry a.u.⁻¹. After full structural relaxation, we obtained the lattice constants $a = b = 10.731$ Å, and $c = 10.687$ Å in the case of excluding SOC while $a = b = 10.732$ Å, and $c = 10.688$ Å when including SOC. For the doped $\text{Cs}_2\text{Ag}_{0.5}\text{Na}_{0.5}\text{InCl}_6$, the structure we used in the DFPT calculations is displayed in Figure 2a.

Supporting Information

Supporting Information is available from the Wiley Online Library or from the author.

Acknowledgements

S.P. and X.L. contributed equally to this work. Z.J. thanks the support from the National Key R&D Program (Grant no. 2017YFA0303401), CAS Interdisciplinary Innovation Team, Beijing Natural Science Foundation (Grant no. JQ18014), NSFC (Grant no.12074371). We thank Dr. Yuanyuan Wu for the XRD discussions.

Conflict of Interest

The authors declare no conflict of interest.

Data Availability Statement

The data that support the findings of this study are available from the corresponding author upon reasonable request.

Keywords

Brillouin light scattering, elastic properties, perovskites, thermal properties

Received: July 28, 2021

Revised: March 7, 2022

Published online: March 23, 2022

- [1] W. N. Du, S. Zhang, Q. Zhang, X. F. Liu, *Adv. Mater.* **2019**, *31*, 1804894.
- [2] F. Yan, J. Xing, G. C. Xing, L. N. Quan, S. T. Tan, J. X. Zhao, R. Su, L. L. Zhang, S. Chen, Y. W. Zhao, A. Huan, E. H. Sargent, Q. H. Xiong, H. V. Demir, *Nano Lett.* **2018**, *18*, 3157.
- [3] H. Y. Fu, *Sol. Energy Mater. Sol. Cells* **2019**, *193*, 107.
- [4] J. B. Li, J. L. Duan, X. Y. Yang, Y. Y. Duan, P. Z. Yang, Q. W. Tang, *Nano Energy* **2021**, *80*, 105526.

- [5] X. Li, X. P. Gao, X. T. Zhang, X. Y. Shen, M. Lu, J. L. Wu, Z. F. Shi, V. L. Colvin, J. H. Hu, X. Bai, W. W. Yu, Y. Zhang, *Adv. Sci.* **2021**, *8*, 2003334.
- [6] F. Igbari, R. Wang, Z. K. Wang, X. J. Ma, Q. Wang, K. L. Wang, Y. Zhang, L. S. Liao, Y. Yang, *Nano Lett.* **2019**, *19*, 2066.
- [7] N. Chen, T. Cai, W. H. Li, K. Hills-Kimball, H. J. Yang, M. D. Que, Y. Nagaoka, Z. Y. Liu, D. Yang, A. G. Dong, C. Y. Xu, R. Zia, O. Chen, *ACS Appl. Mater. Interfaces* **2019**, *11*, 16855.
- [8] J. Yang, C. X. Bao, W. H. Ning, B. Wu, F. X. Ji, Z. B. Yan, Y. T. Tao, J. M. Liu, T. C. Sum, S. Bai, J. P. Wang, W. Huang, W. J. Zhang, F. Gao, *Adv. Opt. Mater.* **2019**, *7*, 1801732.
- [9] W. N. Yuan, G. D. Niu, Y. M. Xian, H. D. Wu, H. M. Wang, H. Yin, P. Liu, W. Z. Li, J. D. Fan, *Adv. Funct. Mater.* **2019**, *29*, 1900234.
- [10] G. Volonakis, A. A. Haghighirad, R. L. Milot, W. H. Sio, M. R. Filip, B. Wenger, M. B. Johnston, L. M. Herz, H. J. Snaith, F. Giustino, *J. Phys. Chem. Lett.* **2017**, *8*, 772.
- [11] J. J. Luo, X. M. Wang, S. R. Li, J. Liu, Y. M. Guo, G. D. Niu, L. Yao, Y. H. Fu, L. Gao, Q. S. Dong, C. Y. Zhao, M. Y. Leng, F. S. Ma, W. X. Liang, L. D. Wang, S. Y. Jin, J. B. Han, L. J. Zhang, J. Etheridge, J. B. Wang, Y. F. Yan, E. H. Sargent, J. Tang, *Nature* **2018**, *563*, 541.
- [12] F. Locardi, E. Sartori, J. Buha, J. Zito, M. Prato, V. Pinchetti, M. L. Zaffalon, M. Ferretti, S. Brovelli, I. Infante, L. De Trizio, L. Manna, *ACS Energy Lett.* **2019**, *4*, 1976.
- [13] Q. S. Hu, G. D. Niu, Z. Zheng, S. R. Li, Y. N. Zhang, H. S. Song, T. Y. Zhai, J. Tang, *Small* **2019**, *15*, 1903496.
- [14] W. J. Zhu, W. B. Ma, Y. R. Su, Z. Chen, X. Y. Chen, Y. G. Ma, L. Z. Bai, W. G. Xiao, T. Y. Liu, H. M. Zhu, X. F. Liu, H. F. Liu, X. Liu, Y. M. Yang, *Light: Sci. Appl.* **2020**, *9*, 112.
- [15] R. T. Williams, K. S. Song, *J. Phys. Chem. Solids* **1990**, *51*, 679.
- [16] Z. L. Yang, X. M. Wang, Y. Z. Chen, Z. F. Zheng, Z. Chen, W. Q. Xu, W. M. Liu, Y. M. Yang, J. Zhao, T. Chen, H. M. Zhu, *Nat. Commun.* **2019**, *10*, 4540.
- [17] W. B. Chu, W. A. Saidi, J. Zhao, O. V. Prezhdo, *Angew. Chem., Int. Ed.* **2020**, *59*, 6435.
- [18] W. B. Chu, Q. J. Zheng, O. V. Prezhdo, J. Zhao, W. A. Saidi, *Sci. Adv.* **2020**, *6*, eaaw7453.
- [19] K. Miyata, T. L. Atallah, X.-Y. Zhu, *Sci. Adv.* **2017**, *3*, e1701469.
- [20] G. Carlotti, L. Doucet, M. Dupeux, *Thin Solid Films* **1997**, *296*, 102.
- [21] Q. Wei, X. J. Li, C. Liang, Z. P. Zhang, J. Guo, G. Hong, G. C. Xing, W. Huang, *Adv. Opt. Mater.* **2019**, *7*, 1900080.
- [22] R. J. Harrison, S. A. T. Redfern, E. K. H. Salje, *Phys. Rev. B* **2004**, *69*, 144101.
- [23] N. Nakamura, H. Ogi, M. Hirao, *Acta Mater.* **2004**, *52*, 765.
- [24] C. Mechri, P. Ruello, J. M. Breteau, M. R. Baklanov, P. Verdonck, V. Gusev, *Appl. Phys. Lett.* **2009**, *95*, 091907.
- [25] A. C. Ferreira, A. Letoublon, S. Paofai, S. Raymond, C. Ecolivet, B. Ruffe, S. Cordier, C. Katan, M. I. Saidaminov, A. A. Zhumekenov, O. M. Bakr, J. Even, P. Bourges, *Phys. Rev. Lett.* **2018**, *121*, 085502.
- [26] S. O. Demokritov, B. Hillebrands, A. N. Slavin, *Phys. Rep.* **2001**, *348*, 441.
- [27] Z. K. Wang, H. S. Lim, S. C. Ng, B. Özyilmaz, M. H. Kuok, *Carbon* **2008**, *46*, 2133.
- [28] R. D. Hartschuh, A. Kisliuk, V. Novikov, A. P. Sokolov, P. R. Heyliger, C. M. Flannery, W. L. Johnson, C. L. Soles, W.-L. Wu, *Appl. Phys. Lett.* **2005**, *87*, 173121.
- [29] D. Faurie, N. Girodon-Boulandet, A. Kaladjian, F. Challali, G. Abadias, P. Djemia, *Rev. Sci. Instrum.* **2017**, *88*, 023903.
- [30] S. Y. Guo, X. L. Huang, S. N. Tkachev, X. P. Fu, J. F. Lin, X. Y. Li, Z. Mao, Q. Zhou, F. F. Li, T. Cui, *Phys. Rev. B* **2018**, *98*, 134107.
- [31] J. M. Lai, Y. R. Xie, J. Zhang, *Nano Res.* **2021**, *14*, 1711.
- [32] S. Baroni, S. de Gironcoli, A. Dal Corso, P. Giannozzi, *Rev. Mod. Phys.* **2001**, *73*, 515.
- [33] J. P. Perdew, K. Burke, M. Ernzerhof, *Phys. Rev. Lett.* **1996**, *77*, 3865.
- [34] J. P. Perdew, A. Zunger, *Phys. Rev. B* **1981**, *23*, 5048.
- [35] M. H. Grimsditch, A. K. Ramdas, *Phys. Rev. B* **1975**, *11*, 3139.
- [36] F. T. Arecchi, E. O. Schulzdu Bois, *Laser Handbook*, Vol. 5, North-Holland, Amsterdam, Netherlands **1972**.
- [37] I. V. Kabakova, I. Azuri, Z. Y. Chen, P. K. Nayak, H. J. Snaith, L. Kronik, C. Paterson, A. A. Bakulin, D. A. Egger, *J. Mater. Chem. C* **2018**, *6*, 3861.
- [38] I. Petousis, D. Mrdjenovich, E. Ballouz, M. Liu, D. Winston, W. Chen, T. Graf, T. D. Schladt, K. A. Persson, F. B. Prinz, *Sci. Data* **2017**, *4*, 160134.
- [39] The Materials Project, <https://materialsproject.org/> (accessed: July 2021).
- [40] N. P. Mathew, N. R. Kumar, R. Radhakrishnan, *Mater. Today: Proc.* **2020**, *33*, 1252.
- [41] I. Khan, Shahab, I. U. Haq, A. Ali, Z. Ali, I. Ahmad, *J. Electron. Mater.* **2021**, *50*, 456.
- [42] Y. R. Xie, S. L. Ren, Y. F. Gao, X. L. Liu, P. H. Tan, J. Zhang, *Sci. China: Phys., Mech. Astron.* **2021**, *64*, 287311.
- [43] M. Born, *Math. Proc. Cambridge Philos. Soc.* **1940**, *36*, 160.
- [44] M. de Jong, W. Chen, R. Notestine, K. Persson, G. Ceder, A. Jain, M. Asta, A. Gamst, *Sci. Rep.* **2016**, *6*, 34256.
- [45] M. de Jong, W. Chen, T. Angsten, A. Jain, R. Notestine, A. Gamst, M. Sluiter, C. K. Ande, S. van der Zwaag, J. J. Plata, C. Toher, S. Curtarolo, G. Ceder, K. A. Persson, M. Asta, *Sci. Data* **2015**, *2*, 150009.
- [46] E. Haque, M. A. Hossain, *Comput. Condens. Matter* **2019**, *19*, e00374.
- [47] E. Haque, M. A. Hossain, *J. Alloys Compd.* **2018**, *748*, 63.
- [48] G. A. Slack, *J. Phys. Chem. Solids* **1973**, *34*, 321.
- [49] C. L. Julian, *Phys. Rev.* **1965**, *137*, A128.
- [50] S. L. Shindé, J. S. Goela, *High Thermal Conductivity Materials*, Springer, New York, USA **2006**.
- [51] T. T. Jia, G. Chen, Y. S. Zhang, *Phys. Rev. B* **2017**, *95*, 155206.
- [52] B. A. Auld, *Acoustic Fields and Waves in Solids. Volume I*, Wiley, New York, USA **1973**.
- [53] R. Vacher, L. Boyer, *Phys. Rev. B* **1972**, *6*, 639.
- [54] Z. J. Wu, E. J. Zhao, H. P. Xiang, X. F. Hao, X. J. Liu, J. Meng, *Phys. Rev. B* **2007**, *76*, 054115.
- [55] O. L. Anderson, *J. Phys. Chem. Solids* **1963**, *24*, 909.
- [56] V. N. Belomestnykh, *Tech. Phys. Lett.* **2004**, *30*, 91.
- [57] D. S. Sanditov, V. N. Belomestnykh, *Tech. Phys.* **2011**, *56*, 1619.
- [58] D. R. Hamann, *Phys. Rev. B* **2013**, *88*, 085117.
- [59] P. Giannozzi, S. Baroni, N. Bonini, M. Calandra, R. Car, C. Cavazzoni, D. Ceresoli, G. L. Chiarotti, M. Cococcioni, I. Dabo, A. Dal Corso, S. de Gironcoli, S. Fabris, G. Fratesi, R. Gebauer, U. Gersann, C. Gougoussis, A. Kokalj, M. Lazzeri, L. Martin-Samos, N. Marzari, F. Mauri, R. Mazzarello, S. Paolini, A. Pasquarello, L. Paulatto, C. Sbraccia, S. Scandolo, G. Sclauzero, A. P. Seitsonen, et al., *J. Phys.: Condens. Matter* **2009**, *21*, 395502.